Materials Science & Engineering A 736 (2018) 12–21

Contents lists available at ScienceDirect

Materials Science & Engineering A

journal homepage: www.elsevier.com/locate/msea

Deformation mechanisms in FCC Co dominated by high-density stacking faults

R. Su[a], D. Neffati[b], S. Xue[a], Q. Li[a], Z. Fan[a], Y. Liu[c], H. Wang[a], Y. Kulkarni[b,*], X. Zhang[a,*]

[a] Department of Materials Engineering, Purdue University, West Lafayette, IN 47907-2045, USA
[b] Department of Mechanical Engineering, University of Houston, Houston, TX 77204-4006, USA
[c] State Key Lab of Metal Matrix Composites, School of Materials Science and Engineering, Shanghai Jiao Tong University, Shanghai 200240, PR China

ARTICLE INFO

Keywords:
Cobalt
In situ compression
Stacking faults
Strain rate sensitivity
Molecular dynamics

ABSTRACT

It has been known that twin boundaries dominate the plasticity of nanotwinned metals. However, the role of stacking faults on the deformation mechanisms in face-centered-cubic (FCC) metals is less well understood. Here we investigate the deformation mechanisms of FCC Co with high-density stacking faults using in situ micropillar compression and atomistic simulations. In situ compression tests show a prominent strain rate dependence, with either strain softening or strain hardening observed at different strain rates. Molecular dynamics simulations reveal that the stacking faults and partial dislocations dominate the plastic deformation of FCC Co. Abundant dislocation junctions form at high strain rate, leading to strengthening.

1. Introduction

Nanotwinned metals have been intensively investigated for the past decade due to their high strength and good ductility [1–24]. Twin boundaries (TBs) can resist the transmission of dislocations to increase strength, accumulate dislocations to accommodate plasticity, and do not scatter electrons as much as regular grain boundaries do to permit high electric conductivity [1,11,20,23,25–38]. Recently, another common planar defect, the stacking fault (SF), has also been studied in materials with hexagonal close packed (HCP) structure [39–41]. Although both TBs and SFs are planar defects and have close connection to partial dislocations, the role of SFs in the mechanical behavior of FCC metals has received little attention [42] compared to the extensive studies on TBs in recent years.

Cobalt (Co) is a widely used material in magnetic data storage devices as well as environmentally sustainable wear and corrosion resistant coatings [43–47]. At room temperature, pure Co has a hexagonal close-packed (HCP) structure. However, we have shown recently that face-centered cubic (FCC) Co can also be stabilized at room temperature by an epitaxial Cu seed layer [48]. Inclined SFs form on (111) planes in FCC Co due to the lattice mismatch between Cu and Co at the interface. The spacing between SFs in FCC Co can be as small as 20–40 nm with large grain size on the order of several microns. However the deformation mechanisms in FCC Co with high-density SFs are not well understood. Furthermore, the formation of high-density SFs in FCC Co provides a unique opportunity to investigate the role of SFs in governing the mechanical response of FCC metals in general.

Several techniques have been developed to investigate the mechanical properties for low dimensional materials. Micropillar compression test developed by Uchic et al. [49] is one of the widely used techniques to study deformability of low dimensional materials [24,50–66]. Size effects, strain rate sensitivity, strain hardening anisotropy, and twin spacing effects have been studied by *ex situ* and in situ pillar compression tests combined with various types of simulations [58,59,61–65,67–76].

In this study, we investigate the mechanical properties of single crystal FCC Co pillar with preexisting high-density inclined SFs by in situ compression tests inside a scanning electron microscope. Under compression, the Co pillars show strain softening and hardening respectively at different strain rates. We combine our experiments with molecular dynamics (MD) simulations to provide atomistic insights into possible deformation mechanisms that may lead to the SF-dominated response observed in our experiments. It is worth mentioning that although most MD simulations are inherently limited by extremely high strain rates (of the order of 10^8/s) and may not be ideal computational tools for studying strain rate dependence, especially at experimentally relevant strain rates [77], these simulations have been successfully applied to explain deformation mechanisms in metallic materials. The purpose of our MD simulations is to elucidate possible SF-mediated deformation mechanisms that may qualitatively explain the strain rate

* Corresponding authors.
E-mail addresses: ykulkarni@uh.edu (Y. Kulkarni), xzhang98@purdue.edu (X. Zhang).

https://doi.org/10.1016/j.msea.2018.08.057
Received 16 March 2018; Accepted 18 August 2018
Available online 20 August 2018
0921-5093/

dependence observed in our experiments. Since there may be atomistic mechanisms that are not entirely captured by MD, we do not draw direct quantitative comparisons but rather rely on qualitative agreement between modeling and experiments.

2. Experimental methods

1 μm thick Co film with 100 nm thick Cu seed layer was deposited on HF etched Si (100) substrates by DC magnetron sputtering. The base pressure of the sputtering chamber was 7×10^{-6} Pa and the deposition rate was ~ 0.3 nm/s for Co. X-ray diffraction (XRD) experiments were performed by using a Bruker D8 Discover X-ray powder diffractometer at room temperature. Transmission electron microscopy (TEM) and high resolution TEM (HRTEM) experiments were performed on an FEI Tecnai T20 and FEI Talos 200X microscope operated at 200 kV. In situ micropillar tests were carried out by using Hysitron PI 88xR PicoIndenter inside an FEI Quanta 3D FEG Dual-beam scanning electron microscope. Single crystal FCC Co pillars with ~ 500 nm diameter were fabricated using the focused-ion-beam (FIB) technique. The height/diameter aspect ratio is ~ 2:1 for all micropillars (Supplementary Fig. S1).

3. Simulation setup

A nanopillar with circular cross-section consisting of a seed layer of FCC Cu and an upper layer of FCC Co was generated for atomistic simulations. The pillar had a diameter of 18.4 nm and the height of the Co layer was 38.4 nm, Thus, the height-to-diameter aspect ratio of the Co pillar for compression study was 2:1. The thickness of the Cu layer was 6 nm. Both layers had the following crystallographic orientation: x: [0 1 $\bar{1}$], y: [0 1 1], z: [1 0 0]. The Co layer consisted of ~ 900,000 atoms. Non-periodic boundary conditions were specified in all directions. The Cu seed layer was made rigid to promote the nucleation of defects in the Co layer. The Cu-Co interactions were modeled using the embedded-atom method (EAM) interatomic potential developed by Zhou et al. [78]. The system was first relaxed at 0 K by conjugate gradient energy minimization and then equilibrated at 300 K for 100 ps using the Nose-Hoover thermostat in the NVT ensemble. The compression simulations were performed at strain rates of 1.37×10^{8}/s and 1.37×10^{9}/s, by keeping the Cu layer fixed and applying a constant velocity to a thin slab of Co, about 2 nm in thickness, at the top. All simulations were performed in LAMMPS [79], and OVITO [80,81] was used for visualization and dislocation analysis.

4. Results

XRD pattern of Co thin film on Si (100) substrate shown in Fig. 1a indicates the epitaxial growth of Cu (200) seed layer and 1 μm thick FCC Co (200). Fig. 1b shows the crystallographic orientation relationship between Si, Cu and Co. Plan-view TEM image of FCC Co examined along [100] zone axis (Fig. 2a) shows arrays of orthogonal high-density SF ribbons. The inserted selected area diffraction (SAD) pattern shows superlattice types of diffraction spots arising from high-density SFs. SF ribbons intersecting at 70° are observed in the cross section TEM (XTEM) micrograph along [110] zone axis (Figs. 2b, 2c). The average spacing between SFs is ~ 25 nm. It is intriguing that SFs initiated from the Cu/Co interface (Fig. 2b) can propagate to the top surface even after intersecting with each other (Fig. 2c). HRTEM micrograph in Fig. 2d shows the details of intersection of two SF ribbons.

To investigate the deformability of FCC Co, we used the FIB technique to fabricate micropillars with ~ 500 nm diameter and ~ 1 μm height and performed systematic in situ micropillar compression tests inside a scanning electron microscope. The stress-strain curves for the micropillars tested at low (1×10^{-3}/s) and high (5×10^{-3}/s) strain rate are different. At low strain rate (1×10^{-3}/s), the yield strength of the micropillar is ~ 700 MPa (red curve shown in Fig. 3a). After a short strain hardening stage (with a strain hardening exponent n of 0.25 ± 0.05) leading to a peak stress of ~ 1100 MPa, the micropillars tested at the low strain rate experience prominent strain softening. In contrast, the micropillars tested at the high strain rate (blue curve shown in Fig. 3a) experience no softening. The yield strength and flow stress plateau are ~ 700 MPa and 1400 MPa, respectively. The strain hardening exponent is 0.35 ± 0.02 for pillars tested at this strain rate. Three pillars were tested at each strain rate, and the strain rate dependent softening and hardening phenomena were reproducible (Supplementary Fig. S2).

Supplementary material related to this article can be found online at doi:10.1016/j.msea.2018.08.057.

In situ SEM snapshots of micropillars at different strains are shown in Figs. 4a and 4b for tests carried out at different strain rates. For the micropillar tested at low strain rate, the pillar deforms uniformly (Fig. 4a). Meanwhile, the pillar tested at higher rate (Fig. 4b) shows classical barreling due to friction stress between indenter tip and pillar top surface. No obvious shear bands are observed in both cases, which will be discussed later.

Jump test was also performed (Fig. 3b) at four different strain rates (5×10^{-4}, 1×10^{-3}, 5×10^{-3} and 1×10^{-2}/s). We found that strain softening occurs at the first two low strain rate regions, followed by strain hardening when strain rate increases to 5×10^{-3}/s or greater. The yield strength of the pillar during the initial jump test is also ~ 700 MPa. The combination of strain softening and strain hardening leads to the surprising V-shape of the true stress-strain curve. In situ SEM snapshots (Fig. 4c) show that the pillar can sustain strain rate jump tests up to ~ 20% of strain without any shear bands or failure.

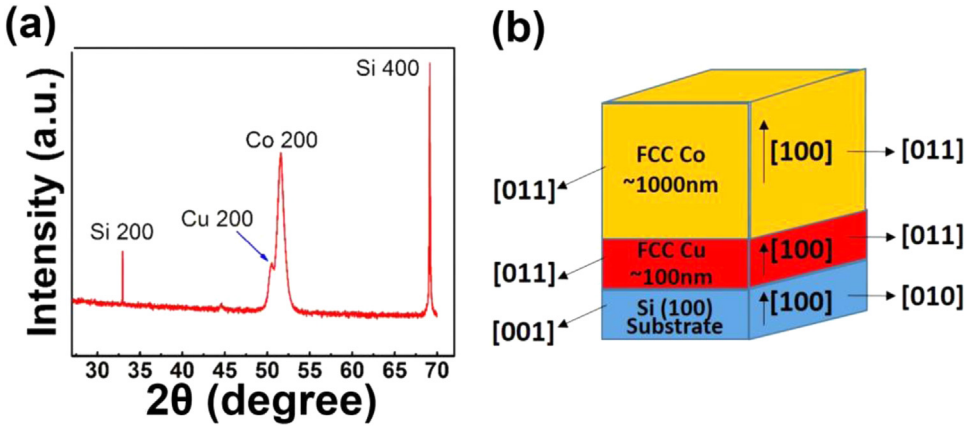

Fig. 1. (a) XRD profiles of 1 μm thick FCC (100) Co film deposited on Si (100) with 100 nm thick Cu seed layer. (b) Crystal orientation relationship between Si substrate, Cu seed and Co film.

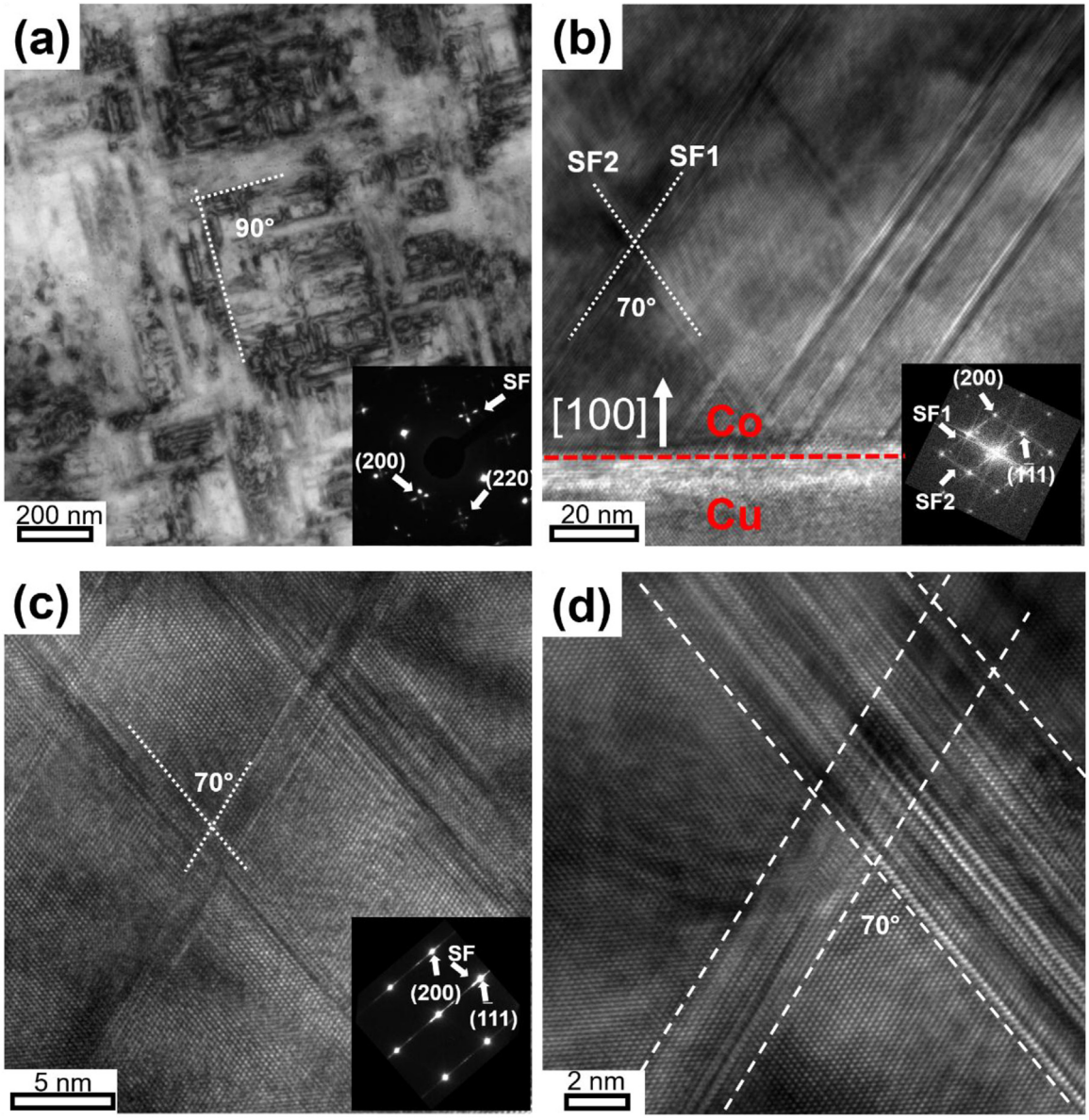

Fig. 2. (a) Plan-view TEM micrograph showing orthogonal stacking fault ribbons from the Co [100] zone axis. The inserted SAD pattern confirms the formation of orthogonal stacking faults. (b) Cross-section TEM (XTEM) micrographs examined from the Co [110] zone axis showing a high density of inclined stacking faults forming a 70° angle, nucleated from the Cu/Co interface. (c) XTEM micrograph shows that the intersecting SF ribbons keep propagating after interception. (d) HRTEM micrograph showing the intersecting SF ribbons before the compression test.

To understand the influence of pre-existing SFs on strengthening of FCC Co, MD simulations of nanopillar compression at different strain rate on FCC Co were performed. As mentioned earlier, 70° inclined and orthogonal SFs are observed at the Cu/Co interfaces (Fig. 5**a**1, 5**a**2), in excellent agreement with our TEM observations. Careful examinations of dislocations near the interface show pairs of 1/6 < 112 > Shockley partials, connected by immobile Hirth locks with Burgers vector of 1/3 < 100 > (Fig. 5a3). Fig. 5b shows the stress-strain curve for the compression simulation performed on the FCC Co/Cu specimen at a strain rate of 1.37×10^8/s. The stress increases rapidly with strain to a maximum of ~ 1.5 GPa, and then decreases and stabilizes at ~ 1 GPa. Based on different deformation mechanisms observed as compression progresses, we divide the stress-strain curve into different regimes (I-V). There appear to be two hardening regions (I and III) and two softening dominated regions (II and IV) with distinct mechanisms and dislocation activities. We also performed a compression simulation at a higher strain rate of 1.37×10^9/s (in Fig. 5c) to do a comparative study of the defect density in the two cases, which will be discussed later. As expected, both cases show similar stress-strain curves since they are both obtained from high strain rates. Hence, the following discussions focus primarily on the MD simulations of nanopillar compression at the lower strain rate and the details on higher strain rate case are shown in the Supplementary information. Atomic structures along with dislocation analyses examined at different strains are shown in Figs. 6 and 7 to gain atomistic insight into the corresponding microstructure evolution. High-resolution movies showing the microstructural evolutions are provided in the supplementary video 4–7.

Supplementary material related to this article can be found online at doi:10.1016/j.msea.2018.08.057.

Initially, the interior of the pillar is relatively free from dislocations (Fig. 6a1) except for the preexisting Shockley partials and Hirth locks formed at the Cu/FCC Co interface. The increase of compressive strain from 0% to 4.6% leads to shortening of the Hirth lock dislocations, which never dissociate into Shockley partials entirely and hence we

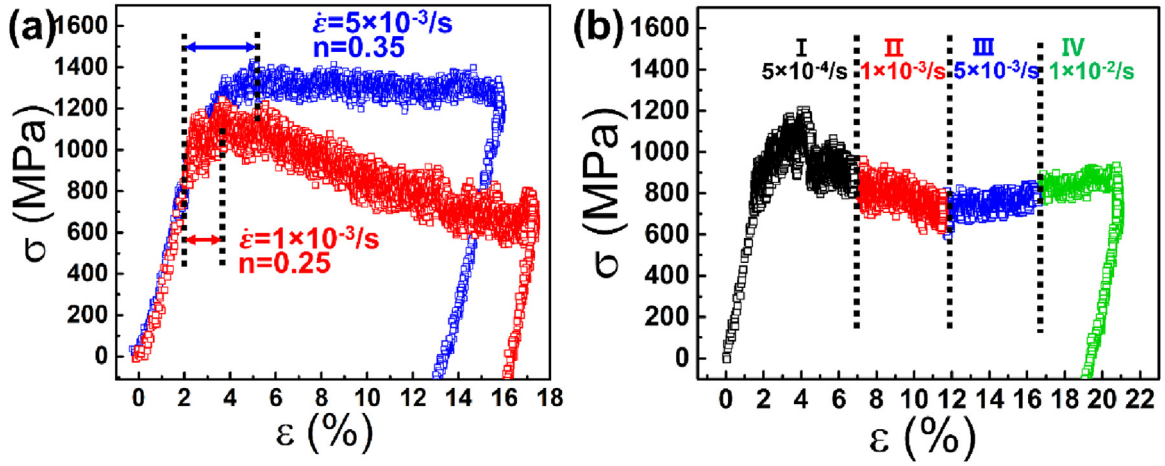

Fig. 3. *In situ* micropillar compression tests of FCC (100) Co at different strain rates. (a) At low strain rate (1×10^{-3}/s, red), the true stress-strain curve shows that shortly after work hardening, the true flow stress decreases gradually with strain - a work softening phenomenon. At high strain rate (5×10^{-3}/s, blue), substantial work hardening is observed after plastic yielding, and flow stress reaches a plateau thereafter. The strain hardening exponent n is 0.25 and 0.35 for compression tests at the two different strain rates. (b) True stress-true strain curves of jump tests at different strain rate (5×10^{-4}/s – 1×10^{-2}/s). Again work softening was observed in FCC Co tested at the strain rate of 5×10^{-4}/s and 1×10^{-3}/s; whereas at higher strain rate, 5×10^{-3}/s and 1×10^{-2}/s, work hardening occurs.

believe that they contribute to the hardening observed in Region I. As these preexisting Shockley partials are restricted by Hirth locks, there are no other mobile dislocations to accommodate deformation, leading to the so-called dislocation starvation induced hardening [50,54,56,82]. At the peak stress (Fig. 6b1), mobile partials are nucleated from the pillar surface. The partials then rapidly propagate and increase the volume fraction of the SFs in the Co pillar (Fig. 6b2–b4), accompanied by rapid stress drop or softening. Figs. 6b3-b4 also show the nucleation of SFs on multiple slip planes and the formation of dislocation locks at the intersections of these SFs. The introduction of these new dislocation locks initiates the hardening observed in regime III. As the plastic deformation continues, the density of SFs and Shockley partials increases dramatically, leading to two consequences. First, subsequent nucleation of intrinsic SFs along existing SFs results in thickened SF ribbons, which limit the migration of dislocations in the FCC structure. Second, the density of sessile dislocations (Hirth locks and stair rod dislocations) increases rapidly. The migration of mobile partial dislocations is significantly inhibited by the intercepting SFs and Hirth locks. During the deformation in region III, 3D views of the snapshots in Figs. 7a1–a4 show the rapid increase of the population of Hirth locks due to the intersecting SFs, and locks and intersections are stable even as the compressive strain increases from 5.49% to 6.5%. The 2D views in Fig. 7a1'–a4′ clearly show interceptions of SFs and HCP laminates.

During deformation in regime IV (corresponding to slight softening observed from strain of 6.6–7.5%), Shockley partials exiting from SF intersections glide along the SF ribbons (appearing as HCP laminates sometimes), leading to the formation of TB (Fig. 7b1–b4). As shown in

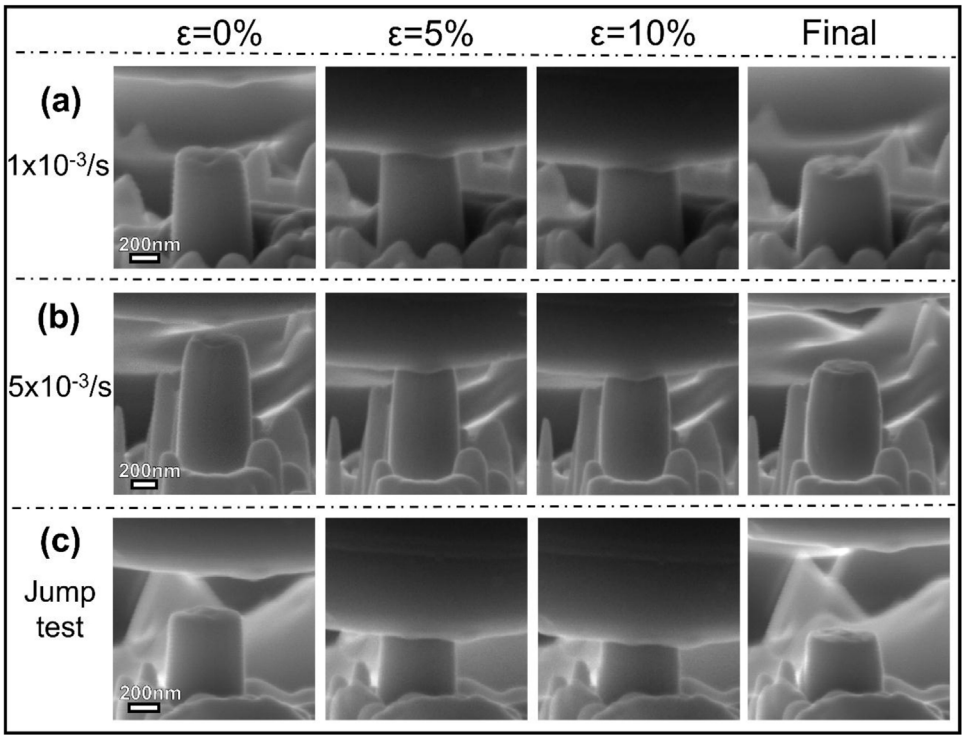

Fig. 4. (a-c) At two different strain rates (1×10^{-3}/s and 5×10^{-3}/s) and jump test, SEM images obtained from in situ compression tests show that the FCC (100) Co pillars show considerable ductility, as evidenced by prominent barreling. (see supplementary Video 1–3 for the evolution of pillar morphology accompanied with stress-strain curves).

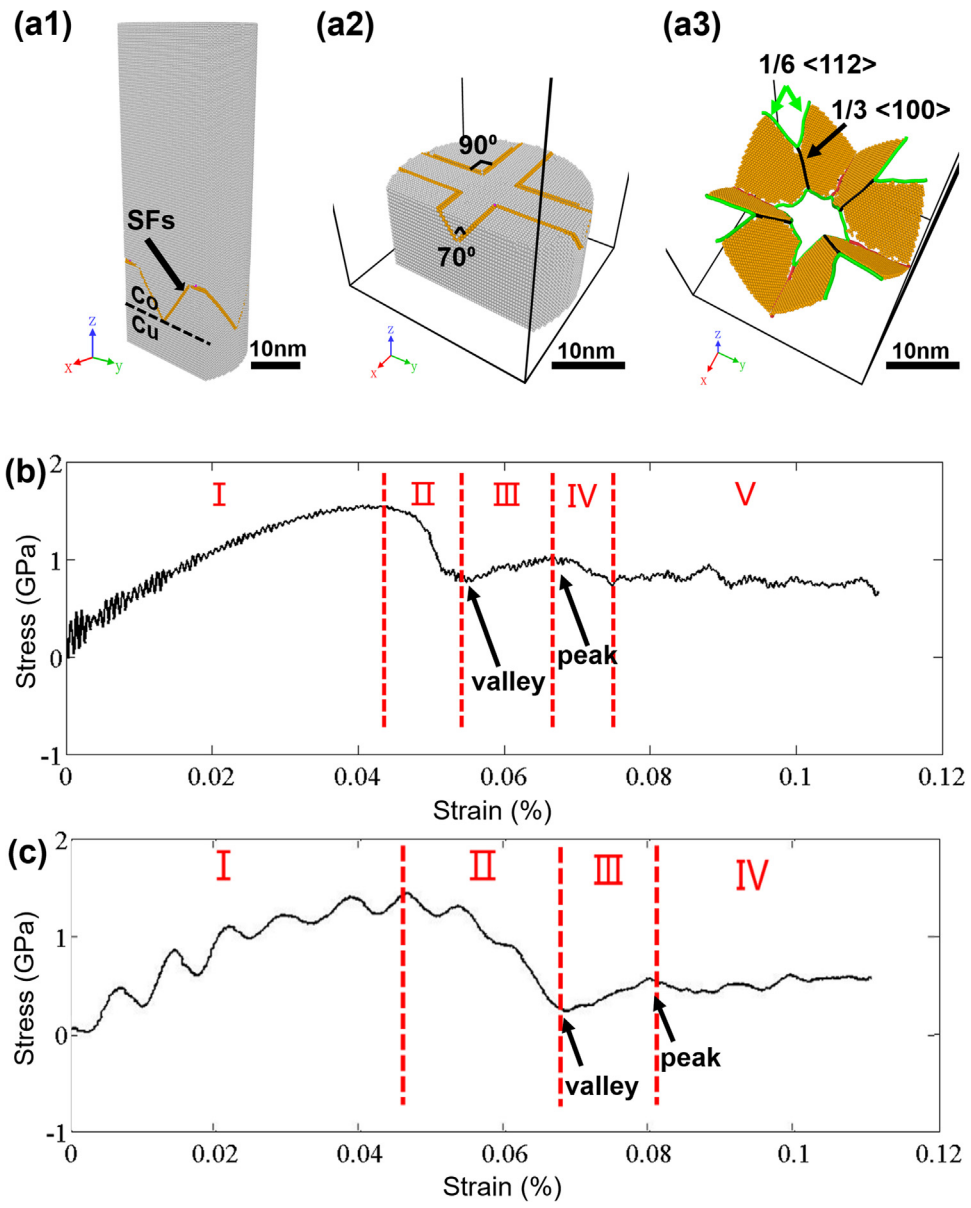

Fig. 5. MD simulation results for compression of a Cu-Co bilayer nanopillar. (a1) SFs initiated from the Cu/Co interface and formed in FCC Co. (a2) The tilted top-down view of initial SFs formed in FCC Co. (a3) Shockley partials (marked in green color) and Hirth locks (**b** $=1/3<100>$, marked in black color) generated after energy minimization. (b) The stress-strain curve for nanopillar compression at a strain rate of 1.37×10^{8}/s. The flow stress increases rapidly to ~ 1.5 GPa, and decreases thereafter to ~ 1 GPa. A sequence of hardening and softening is observed in four main regimes denoted by I-IV. The associated deformation mechanisms are identified by comparing the microstructures and defects evolutions at different regions. Quantitative dislocation analyses are performed on valley and peak stress in Region III. (c) The stress-strain curve for nanopillar compression at a strain rate of 1.37×10^{9}/s. Quantitative dislocation analyses are performed at the valley and peak stress as indicated in Region III.

Fig. 7b2'–b4', continuous migration of Shockley partials along the TB leads to TB migration along the normal direction. This process can be directly observed from in supplementary video 7.

5. Discussion

5.1. The formation of high-density intersecting SFs in FCC Co

Epitaxial growth of FCC Co on Cu (100) has been reported before [44,48]. In general, a very thin layer of FCC Co (50 nm) may form on Cu buffer layer [44]. Beyond this thickness, Co should transform from FCC to HCP phase. This is indeed the case when Co grows on Cu (111) seed layers [48]. However in the current study, we identified the stabilization of ultra-thick FCC Co (100), 1 μm in thickness, which is quite surprising. Groups of Shockley partials nucleate from the Cu/FCC Co layer interface (Fig. 2b) to alleviate the 2.6% lattice mismatch strain between Cu and Co. These SFs can reinitiate after intersecting with other SFs and propagate throughout the entire film, and thus can alleviate the mismatch strain in the entire film to stabilize the thick FCC Co film. This reinitiation process is also confirmed by MD simulations. Meanwhile, a $1/3<100>$ Hirth lock is left at the intersection of SFs. These preexisting Hirth locks play an important role in strengthening mechanism, which is discussed next.

5.2. Strengthening and softening mechanisms in FCC Co revealed by MD simulations

MD simulations show that the deformation in FCC Co is dominated by the activity of partial dislocations. This is possibly due to the low stacking fault energy (SFE) of FCC Co, which is calculated to be -51 mJ/m^2 using the same interatomic potential [78]. The negative SFE value is also predicted by a previous study [83]. Furthermore MD simulations suggest two types of hardening and softening mechanisms occurring in four regions. The dislocation starvation induced hardening during initial loading in Region I is somewhat surprising as there are preexisting Shockley partials due to the mismatch strain between Cu and FCC Co. However, these Shockley partials cannot migrate as they are constrained by Hirth locks. MD simulations indeed reveal the shortening of Hirth locks during initial loading, but Shockley partials remain tied to the Hirth Locks. Hardening continues until the avalanche of dislocations due to nucleation of partials and SFs from surface. Such an avalanche of dislocations leads to drastic softening in Region II.

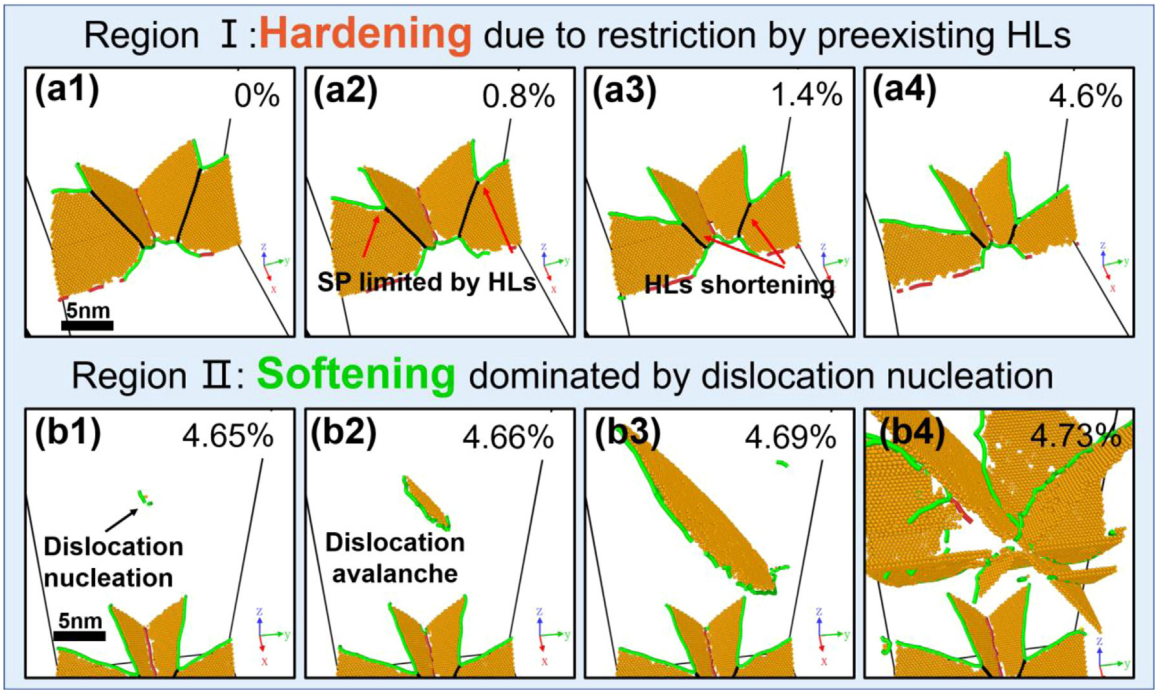

Fig. 6. Evolutions of atomistic configurations at different strains during Region I and II illustrated in OVITO using common neighbor analysis. FCC atoms are colored in grey, HCP atoms are colored in gold, BCC atoms are colored in pink and other atoms are colored in green. Using dislocation analysis, the green lines show Shockley partials (SP), Hirth locks (HL) are colored in black, and the red lines show dislocations with other Burgers vectors. (a1–a4) The restriction imposed by the Hirth locks on the pre-existing Shockley partials leading to starvation of mobile dislocations in region I. (b1–b4) The avalanche of partial dislocations from the surface leads to rapid increase of thin SF ribbons in the softening region II. (See supplementary video 4 and 5 for more details.).

The second type of hardening mechanism revealed by MD is due to the interception of SFs formed in the previous region and formation of new Hirth locks at a greater strain level (Region III). Continuous deformation leads to thickening of SF ribbons (HCP laminates) during deformation in region I and II due to nucleation of a significant number of SFs. These HCP laminates as well as SFs play a similar role as TBs or grain boundaries in limiting dislocation transmission and thus contribute to strengthening and work hardening.

The second type of softening mechanisms in Region IV is intriguing. It appears that mobile Shockley partials escape from the interception between certain thin SFs and HCP laminates. These partials migrate along the SF ribbons and lead to the gradual defaulting of HCP laminate to eventually form a TB. Further migration of Shockley partials along the TB results in the normal motion or migration of the TB along its normal direction. The migration of TBs under deformation of nanotwinned metals has been reported previously [84]. Using MD simulations Li et al [7] revealed softening in nanotwinned Cu due to the transition from dislocation pile-up mechanisms to partial dominated TB migrations in extremely fine (1 nm or less) twinned Cu. Zhu et al. [85] reported the constriction of partials and subsequent absorption (spread) of the full dislocation along TBs in twinned Cu. It is worth mentioning that the second type of softening mechanism observed here is less drastic compared to the first type of softening, where the avalanche of dislocations occurs.

Finally, we would like to emphasize that even if the hardening and softening observed in regions III and IV in MD simulations are not very significant (limited by high strain rate), the different atomistic mechanisms that can lead to a hardening or softening response provide qualitative support for the strain rate dependent hardening and softening observed in our experiments.

5.3. Strain rate dependent deformation mechanisms in FCC Co with SFs

We now attempt to interpret the strain rate dependent deformation behavior of FCC Co observed in our experiments. For the Co pillar tested at low strain rate (1×10^{-3}/s), yield strength is $\sim$ 700 MPa, followed by a transient work hardening stage. Although Hirth Locks in the as-deposited films may be strong barriers for the release of mobile partials, a dislocation starvation dominated hardening mechanism alone, as predicted by MD simulations, may not explain the work hardening observed experimentally, because the specimen dimension is much larger than that used in MD simulation, and it is less likely that all preexisting Shockley partials are constrained by Hirth locks. The second type of hardening due to blocking of SFs by HCP laminates may be a more realistic work hardening mechanism. It follows that the gradual softening observed at low strain rate may be a consequence of dissociation of Hirth lock and activation of abundant partials that glide along SFs. Our calculation in Supplementary materials reveals that the critical stress to dissociate Hirth locks is $\sim$ 1.15 GPa, which is close to the peak stress measured at low strain rate during in situ compression tests. MD simulations show that the activation of mobile Shockley partials stems from certain interceptions where Hirth locks did not form. Furthermore, these mobile partials gradually reduce the thickness of SFs via a defaulting process, resulting in a lower density of SF ribbons (HCP laminates).

Prior studies show that dislocations in single crystal pillars or nanowires may exit the free surface [50,52,54,82]. Due to the inability to accumulate internal dislocations, there is a lack of work hardening in these nanowires, and consequently they exhibit either softening or brittle fracture [54,86]. In sub-micron size single crystal Ni and Al pillars, similar softening phenomenon has been observed because dislocation recovery rate exceeds the dislocation nucleation rate [54,87]. Note that at low strain rate, though strain softening occurs, the FCC Co pillar remains uniformly deformed as shown by in situ compression studies.

When the strain rate is increased to 5×10^{-3}/s, the micropillar exhibits no strain softening. A prominent strain hardening is observed until the stress reaches a plateau, $\sim$ 1.4 GPa. Plastic yielding occurs at

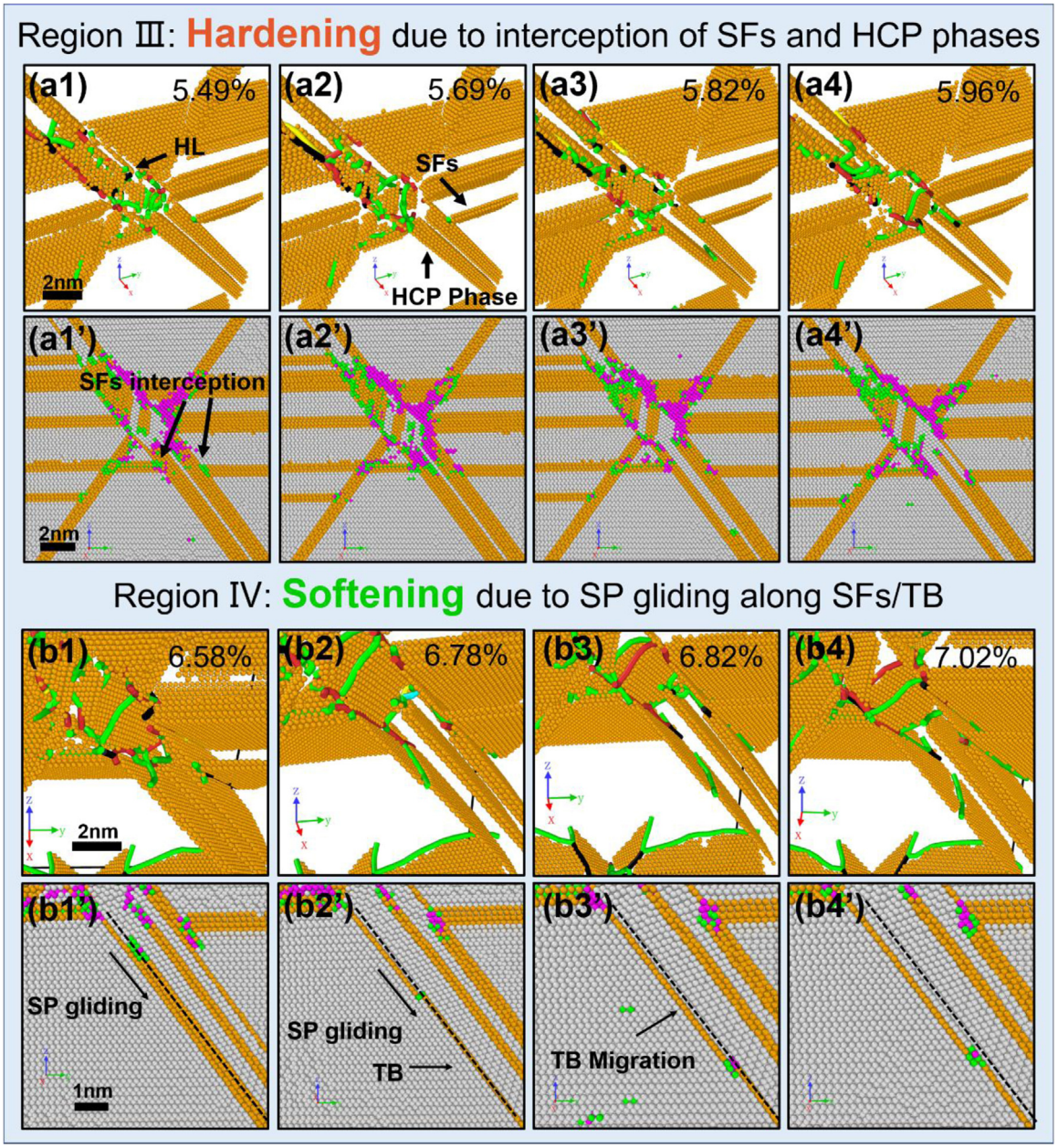

Fig. 7. Evolutions of atomistic configurations at different strains during Region III and IV illustrated in OVITO using common neighbor analysis. (a1-a4) In region III (hardening), 3D snap shots showing the interception of SFs lead to the formation of sessile locks, and the thickening of SFs leads to the increase of fraction of HCP laminates. (a1′-a4′) The corresponding 2D views show that HCP laminates hinder the penetration of intersecting SFs. (b1-b4) During deformation in region IV, 3D snapshots show that after a SF is blocked by an HCP laminate, the Shockley partial from the SF start gliding along the HCP phase, leading to gradual defaulting and translate the HCP laminate into a TB. (b1′-b4′) 2D snap shots show that the continuous migration of partial on the TB leads to the migration of the TB downward. The black dash line shows the original position of the TB plane. (See supplemental video 6 and 7 for more details.).

~ 700 MPa, indicating that the stress necessary to move mobile partials is similar to that of the pillar deformed at lower rate. At higher strain rate, more mobile partial dislocations are nucleated to accommodate plastic deformation. In general when dislocation nucleation rate is greater than dislocation consumption rate, strain hardening would prevail [87]. In this case, when the density of partial dislocations increases, the chances for Shockley partials to intersect with each other also increase, and thus the probability of forming Hirth locks would also increase.

To test this hypothesis, we performed another MD compression simulation at a higher strain rate (1.37×10^9/s). The stress-strain curve for this simulation shown in Fig. 5c reveals a similar trend: two strengthening regions followed by two softening regions. Dislocation analyses of the two pillars subjected to different stain rates are shown in Fig. 8a and b. For both cases, we choose the atomistic configurations at the lowest (valley) stress (Fig. 8a1 and b1) and highest (peak) stress (Fig. 8a2 and b2) in region III to compare the dislocation structures. We find that the density and number of segments of Hirth locks both increase with increasing stress, which consolidates the role of Hirth locks as a dislocation barrier and their contribution to strain hardening (Fig. 8c and d). Also at higher strain rate, the density and number of segments of Hirth locks are more than two times greater than those at lower strain rate. This analysis also verifies our hypothesis that a higher strain rate increases the number of Hirth locks, hence promotes strain hardening. Finally, macroscopically when dislocation nucleation and recovery rate reach a balance, the flow stress is maintained at

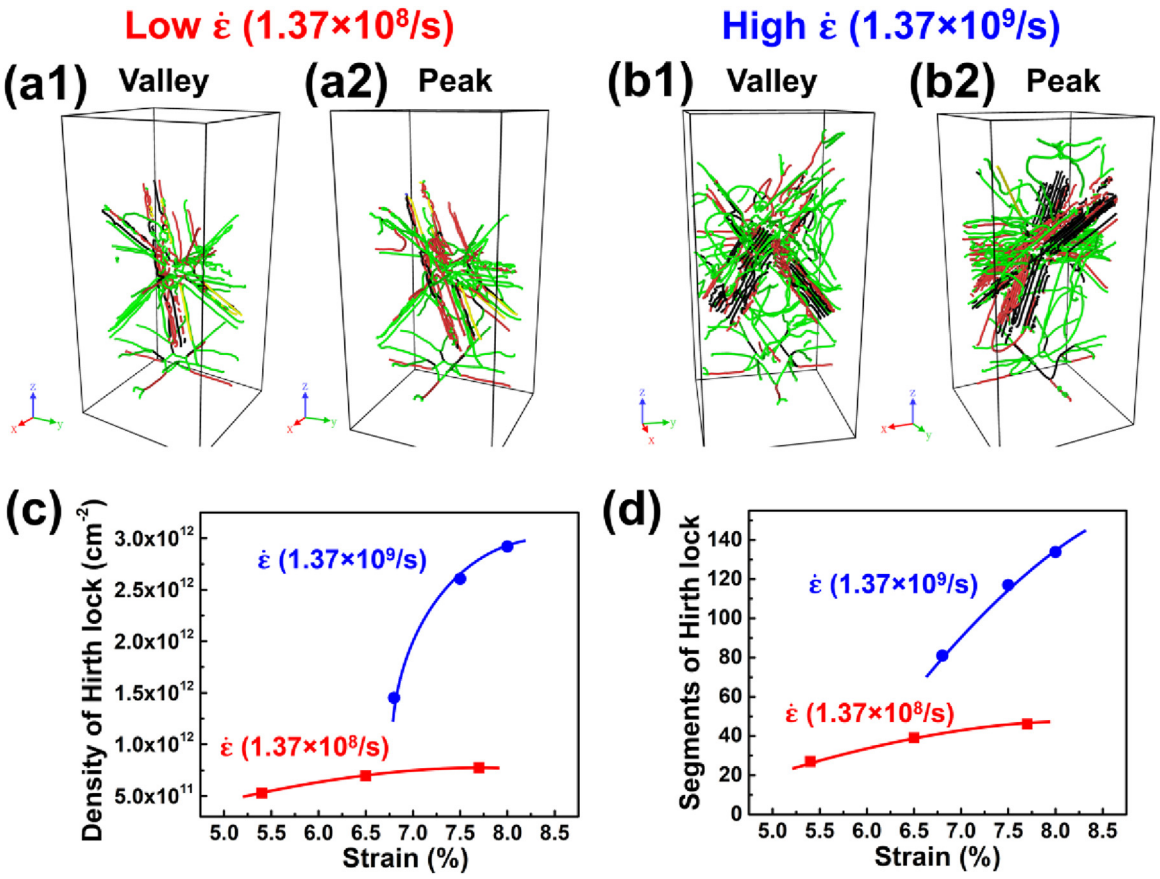

Fig. 8. Dislocation analysis of the MD simulations performed at relatively low (1.37×10^8/s) and high (1.37×10^9/s) strain rate (a, b). (a1-a2) The dislocation lines observed at low strain rate at lowest stress (valley) and highest stress (peak) in region III (see Fig. 5b) respectively. (b1-b2) The dislocation lines observed at high strain rate at the valley and peak stress in region III (see Fig. 5c) respectively. (c) The density of Hirth locks increases with strain rate at valley and peak stress. (d) The number of Hirth lock segments also increases with increasing strain rate.

~ 1.4 GPa. Foregoing interpretation also works well for the experimental compressive jump test performed at various strain rates (Fig. 3b), which leads to a unique V-shape stress-strain curve. The pillar tested during the jump tests also deformed uniformly up to ~ 20% strain (Fig. 4c).

In general, FCC single crystal pillars with submicron pillar size, such as Au [82], Cu [62,69], Ni [54] and Al [86], often experience intermittent strain bursts or serrated yielding during deformation. This plastic instability is an intrinsic characteristic of micrometer size single crystal metals, due to dislocation avalanches. However, instead of intermittent strain burst, single crystal FCC Co with high-density intersecting SFs exhibits significant work hardening and smooth stress-strain curve. The inclined SF ribbons (HCP laminates) block the transmission of partial dislocations and prohibit the formation of dislocation avalanches, which can only be accomplished previously by increasing pillar size in single crystal FCC metals [62,88]. Also in contrast to the uniform deformation at low strain rate, in situ micropillar compression tests show barreling at higher strain rate, which is a manifestation of strain hardening in FCC Co due to the formation of a greater density of dislocations and Hirth locks inside the pillar as suggested by MD simulations discussed previously.

6. Conclusions

In conclusion, we report on an intriguing SF dominated deformation mechanism, which is also sensitive to strain rate in single crystal FCC Co (100) pillar. The phenomenon of strain softening at low strain rate arises from insufficient density of intersections or Hirth locks and the propagation of partials along SF ribbons. In contrast, at higher strain rate, abundant Hirth locks and SF intersections can effectively inhibit the migration of partials, leading to substantial work hardening. The smooth stress-strain curve and homogenous morphology variation associated with the deformed pillars indicate that SFs can also prohibit strain burst and enhance plasticity. MD simulations furnish atomistic insights into the possible SF-mediated deformation mechanisms at play and provide support for the contribution of SF ribbons (HCP laminates) and Hirth locks to strain hardening and SF dominated plasticity. The conclusions derived from the combination of experimental and computational studies may stimulate significant interest in the stacking-fault dominated strengthening and plasticity in metallic materials.

Acknowledgement

RS and XZ acknowledge the financial support by NSF-DMR 1642759. DN and YK acknowledge the financial support by NSF-DMR 1508484. Fabrication of micropillars by SX and QL are supported by DOE-BES under Grant no. DE-SC0016337. H. Wang acknowledges the support from the U.S. Office of Naval Research (N00014-16-1-2778). Access to the Life Sciences Microscopy Center and Materials Science Microscopy Center at Purdue University are also acknowledged. The support from the Center of Advanced Computing and Data Systems at the University of Houston is also acknowledged.

Appendix A. Supplementary material

Supplementary data associated with this article can be found in the online version at doi:10.1016/j.msea.2018.08.057.

References

[1] L. Lu, Y. Shen, X. Chen, L. Qian, K. Lu, Ultrahigh strength and high electrical conductivity in copper, Science 304 (5669) (2004) 422–426.
[2] X. Zhang, A. Misra, H. Wang, A.L. Lima, M.F. Hundley, R.G. Hoagland, Effects of deposition parameters on residual stresses, hardness and electrical resistivity of nanoscale twinned 330 stainless steel thin films, J. Appl. Phys. 97 (9) (2005).
[3] X. Zhang, H. Wang, X.H. Chen, L. Lu, K. Lu, R.G. Hoagland, A. Misra, High-strength sputter-deposited Cu foils with preferred orientation of nanoscale growth twins, Appl. Phys. Lett. 88 (17) (2006).
[4] X.H. Chen, L. Lu, Work hardening of ultrafine-grained copper with nanoscale twins, Scr. Mater. 57 (2) (2007) 133–136.
[5] B. Li, B.Y. Cao, K.T. Ramesh, E. Ma, A nucleation mechanism of deformation twins in pure aluminum, Acta Mater. 57 (15) (2009) 4500–4507.
[6] O. Anderoglu, A. Misra, J. Wang, R.G. Hoagland, J.P. Hirth, X. Zhang, Plastic flow stability of nanotwinned Cu foils, Int. J. Plast. 26 (6) (2010) 875–886.
[7] X. Li, Y. Wei, L. Lu, K. Lu, H. Gao, Dislocation nucleation governed softening and maximum strength in nano-twinned metals, Nature 464 (7290) (2010) 877–880.
[8] N. Li, J. Wang, J.Y. Huang, A. Misra, X. Zhang, Influence of slip transmission on the migration of incoherent twin boundaries in epitaxial nanotwinned Cu, Scr. Mater. 64 (2) (2011) 149–152.
[9] D. Bufford, H. Wang, X. Zhang, High strength, epitaxial nanotwinned Ag films, Acta Mater. 59 (1) (2011) 93–101.
[10] A.M. Hodge, T.A. Furnish, A.A. Navid, T.W. Barbee Jr., Shear band formation and ductility in nanotwinned Cu, Scr. Mater. 65 (11) (2011) 1006–1009.
[11] N. Li, J. Wang, A. Misra, X. Zhang, J.Y. Huang, J.P. Hirth, Twinning dislocation multiplication at a coherent twin boundary, Acta Mater. 59 (15) (2011) 5989–5996.
[12] N. Li, J. Wang, X. Zhang, A. Misra, In-situ TEM study of dislocation-twin boundaries interaction in nanotwinned Cu films, JOM 63 (9) (2011) (62-U62).
[13] D. Bufford, Z. Bi, Q.X. Jia, H. Wang, X. Zhang, Nanotwins and stacking faults in high-strength epitaxial Ag/Al multilayer films, Appl. Phys. Lett. 101 (22) (2012).
[14] D. Bufford, H. Wang, X. Zhang, Thermal stability of twins and strengthening mechanisms in differently oriented epitaxial nanotwinned Ag films, J. Mater. Res. 28 (13) (2013) 1729–1739.
[15] D. Bufford, Y. Liu, Y. Zhu, Z. Bi, Q.X. Jia, H. Wang, X. Zhang, Formation mechanisms of high-density growth twins in aluminum with high stacking-fault energy, Mater. Res. Lett. 1 (1) (2013) 51–60.
[16] D. Bufford, Y. Liu, J. Wang, H. Wang, X. Zhang, In situ nanoindentation study on plasticity and work hardening in aluminium with incoherent twin boundaries, Nat. Commun. 5 (2014) 4864.
[17] Y. Liu, J. Jian, Y. Chen, H. Wang, X. Zhang, Plasticity and ultra-low stress induced twin boundary migration in nanotwinned Cu by in situ nanoindentation studies, Appl. Phys. Lett. 104 (23) (2014) 231910.
[18] J. Li, Y. Chen, S. Xue, H. Wang, X. Zhang, Comparison of size dependent strengthening mechanisms in Ag/Fe and Ag/Ni multilayers, Acta Mater. 114 (2016) 154–163.
[19] M. Lentz, M. Risse, N. Schaefer, W. Reimers, I.J. Beyerlein, Strength and ductility with {10(1)over-bar1} - {10(1)over-bar2} double twinning in a magnesium alloy, Nat. Commun. 7 (2016) 7.
[20] M. Ardeljan, I.J. Beyerlein, M. Knezevic, Effect of dislocation density-twin interactions on twin growth in AZ31 as revealed by explicit crystal plasticity finite element modeling, Int. J. Plast. 99 (2017) 81–101.
[21] S. Zheng, I.J. Beyerlein, J.S. Carpenter, K. Kang, J. Wang, W. Han, N.A. Mara, High-strength and thermally stable bulk nanolayered composites due to twin-induced interfaces, 4 (2013) 1696.
[22] F. Sansoz, K. Lu, T. Zhu, A. Misra, Strengthening and plasticity in nanotwinned metals, MRS Bull. 41 (4) (2016) 292–297.
[23] Z. Zeng, X. Li, L. Lu, T. Zhu, Fracture in a thin film of nanotwinned copper, Acta Mater. 98 (2015) 313–317.
[24] A. Kobler, T. Beuth, T. Klöffel, R. Prang, M. Moosmann, T. Scherer, S. Walheim, H. Hahn, C. Kübel, B. Meyer, T. Schimmel, E. Bitzek, Nanotwinned silver nanowires: structure and mechanical properties, Acta Mater. 92 (Suppl. C) (2015) S299–S308.
[25] J. Wang, H.C. Huang, Shockley partial dislocations to twin: another formation mechanism and generic driving force, Appl. Phys. Lett. 85 (24) (2004) 5983–5985.
[26] Z.H. Jin, P. Gumbsch, E. Ma, K. Albe, K. Lu, H. Hahn, H. Gleiter, The interaction mechanism of screw dislocations with coherent twin boundaries in different face-centred cubic metals, Scr. Mater. 54 (6) (2006) 1163–1168.
[27] A.J. Cao, Y.G. Wei, S.X. Mao, Deformation mechanisms of face-centered-cubic metal nanowires with twin boundaries, Appl. Phys. Lett. 90 (15) (2007).
[28] C. Deng, F. Sansoz, Enabling ultrahigh plastic flow and work hardening in twinned gold nanowires, Nano Lett. 9 (4) (2009) 1517–1522.
[29] J. Wang, X. Zhang, Twinning effects on strength and plasticity of metallic materials, MRS Bull. 41 (4) (2016) 274–281.
[30] H. Wang, P.D. Wu, J. Wang, C.N. Tomé, A crystal plasticity model for hexagonal close packed (HCP) crystals including twinning and de-twinning mechanisms, Int. J. Plast. 49 (Suppl. C) (2013) S36–S52.
[31] D.W. Brown, I.J. Beyerlein, T.A. Sisneros, B. Clausen, C.N. Tomé, Role of twinning and slip during compressive deformation of beryllium as a function of strain rate, Int. J. Plast. 29 (Supplement C) (2012) S120–S135.
[32] S.R. Niezgoda, A.K. Kanjarla, I.J. Beyerlein, C.N. Tomé, Stochastic modeling of twin nucleation in polycrystals: an application in hexagonal close-packed metals, Int. J. Plast. 56 (Suppl. C) (2014) S119–S138.
[33] G.J. Tucker, S.M. Foiles, Quantifying the influence of twin boundaries on the deformation of nanocrystalline copper using atomistic simulations, Int. J. Plast. 65 (2015) 191–205.
[34] P. Chowdhury, H. Sehitoglu, H.J. Maier, R. Rateick, Strength prediction in NiCo alloys – the role of composition and nanotwins, Int. J. Plast. 79 (Supplement C) (2016) 237–258.
[35] X. Xiao, D. Song, H. Chu, J. Xue, H. Duan, Mechanical behaviors of irradiated FCC polycrystals with nanotwins, Int. J. Plast. 74 (Suppl. C) (2015) S110–S126.
[36] Y. Liu, N. Li, D. Bufford, J.H. Lee, J. Wang, H. Wang, X. Zhang, In situ nanoindentation studies on detwinning and work hardening in nanotwinned monolithic metals, JOM 68 (1) (2016) 127–135.
[37] H. Zhou, X. Li, S. Qu, W. Yang, H. Gao, A. Jogged Dislocation, Governed strengthening mechanism in nanotwinned metals, Nano Lett. 14 (9) (2014) 5075–5080.
[38] Y.M. Wang, F. Sansoz, T. LaGrange, R.T. Ott, J. Marian, T.W. Barbee Jr, A.V. Hamza, Defective twin boundaries in nanotwinned metals, Nat. Mater. 12 (8) (2013) 697–702.
[39] S. Sandlöbes, M. Friák, S. Zaefferer, A. Dick, S. Yi, D. Letzig, Z. Pei, L.F. Zhu, J. Neugebauer, D. Raabe, The relation between ductility and stacking fault energies in Mg and Mg–Y alloys, Acta Mater. 60 (6–7) (2012) 3011–3021.
[40] W.W. Jian, G.M. Cheng, W.Z. Xu, C.C. Koch, Q.D. Wang, Y.T. Zhu, S.N. Mathaudhu, Physics and model of strengthening by parallel stacking faults, Appl. Phys. Lett. 103 (13) (2013) 133108.
[41] W.W. Jian, G.M. Cheng, W.Z. Xu, H. Yuan, M.H. Tsai, Q.D. Wang, C.C. Koch, Y.T. Zhu, S.N. Mathaudhu, Ultrastrong Mg alloy via nano-spaced stacking faults, Mater. Res. Lett. 1 (2) (2013) 61–66.
[42] P. Wang, S. Xu, J. Liu, X. Li, Y. Wei, H. Wang, H. Gao, W. Yang, Atomistic simulation for deforming complex alloys with application toward TWIP steel and associated physical insights, J. Mech. Phys. Solids 98 (2017) 290–308.
[43] F. Huang, M.T. Kief, G.J. Mankey, R.F. Willis, Magnetism in the few-monolayers limit: a surface magneto-optic Kerr-effect study of the magnetic behavior of ultrathin films of Co, Ni, and Co-Ni alloys on Cu(100) and Cu(111), Phys. Rev. B 49 (6) (1994) 3962–3971.
[44] R. Naik, C. Kota, J.S. Payson, G.L. Dunifer, Ferromagnetic-resonance studies of epitaxial Ni, Co, and Fe films grown on Cu(100)/Si(100), Phys. Rev. B 48 (2) (1993) 1008–1013.
[45] P.F. Carcia, A.D. Meinhaldt, A. Suna, Perpendicular magnetic anisotropy in Pd/Co thin film layered structures, Appl. Phys. Lett. 47 (2) (1985) 178–180.
[46] A. Chiba, K. Kumagai, N. Nomura, S. Miyakawa, Pin-on-disk wear behavior in a like-on-like con`uration in a biological environment of high carbon cast and low carbon forged Co–29Cr–6Mo alloys, Acta Mater. 55 (4) (2007) 1309–1318.
[47] M. Srivastava, V. Ezhil Selvi, V.K. William Grips, K.S. Rajam, Corrosion resistance and microstructure of electrodeposited nickel–cobalt alloy coatings, Surf. Coat. Technol. 201 (6) (2006) 3051–3060.
[48] Y. Liu, Y. Chen, K. Yu, H. Wang, J. Chen, X. Zhang, Stacking fault and partial dislocation dominated strengthening mechanisms in highly textured Cu/Co multilayers, Int. J. Plast. 49 (2013) 152–163.
[49] M.D. Uchic, D.M. Dimiduk, J.N. Florando, W.D. Nix, Sample dimensions influence strength and crystal plasticity, Science 305 (5686) (2004) 986–989.
[50] J.R. Greer, W.C. Oliver, W.D. Nix, Size dependence of mechanical properties of gold at the micron scale in the absence of strain gradients, Acta Mater. 53 (6) (2005) 1821–1830.
[51] H. Bei, S. Shim, E.P. George, M.K. Miller, E.G. Herbert, G.M. Pharr, Compressive strengths of molybdenum alloy micro-pillars prepared using a new technique, Scr. Mater. 57 (5) (2007) 397–400.
[52] H. Tang, K.W. Schwarz, H.D. Espinosa, Dislocation escape-related size effects in single-crystal micropillars under uniaxial compression, Acta Mater. 55 (5) (2007) 1607–1616.
[53] K.S. Ng, A.H.W. Ngan, Stochastic nature of plasticity of aluminum micro-pillars, Acta Mater. 56 (8) (2008) 1712–1720.
[54] Z.W. Shan, R.K. Mishra, S.A.S. Asif, O.L. Warren, A.M. Minor, Mechanical annealing and source-limited deformation in submicrometre-diameter Ni crystals, Nat. Mater. 7 (2) (2008) 115–119.
[55] H. Tang, K.W. Schwarz, H.D. Espinosa, Dislocation-source shutdown and the plastic behavior of single-crystal micropillars, Phys. Rev. Lett. 100 (18) (2008).
[56] J.R. Greer, J.-Y. Kim, M.J. Burek, The in-situ mechanical testing of nanoscale single-crystalline nanopillars, JOM 61 (12) (2009) 19–25.
[57] A.T. Jennings, M.J. Burek, J.R. Greer, Microstructure versus Size: mechanical properties of electroplated single crystalline Cu nanopillars, Phys. Rev. Lett. 104 (13) (2010).
[58] S. Akarapu, H.M. Zbib, D.F. Bahr, Analysis of heterogeneous deformation and dislocation dynamics in single crystal micropillars under compression, Int. J. Plast. 26 (2) (2010) 239–257.
[59] J.-Y. Kim, D. Jang, J.R. Greer, Crystallographic orientation and size dependence of tension–compression asymmetry in molybdenum nano-pillars, Int. J. Plast. 28 (1) (2012) 46–52.
[60] B.-G. Yoo, J.-Y. Kim, Y.-J. Kim, I.-C. Choi, S. Shim, T.Y. Tsui, H. Bei, U. Ramamurty, J.-I. Jang, Increased time-dependent room temperature plasticity in metallic glass nanopillars and its size-dependency, Int. J. Plast. 37 (Suppl. C) (2012) S108–S118.
[61] R. Soler, J.M. Molina-Aldareguia, J. Segurado, J. Llorca, R.I. Merino, V.M. Orera, Micropillar compression of LiF [111] single crystals: effect of size, ion irradiation and misorientation, Int. J. Plast. 36 (Suppl. C) (2012) S50–S63.
[62] J.Y. Zhang, G. Liu, J. Sun, Strain rate effects on the mechanical response in multi- and single-crystalline Cu micropillars: grain boundary effects, Int. J. Plast. 50 (2013) 1–17.
[63] R. Gu, A.H.W. Ngan, Size-dependent creep of duralumin micro-pillars at room temperature, Int. J. Plast. 55 (Suppl. C) (2014) S219–231.
[64] P. Lin, Z. Liu, Z. Zhuang, Numerical study of the size-dependent deformation morphology in micropillar compressions by a dislocation-based crystal plasticity

model, Int. J. Plast. 87 (Suppl. C) (2016) S32–S47.
[65] J. Zhang, K. Kishida, H. Inui, Specimen size and shape dependent yield strength in micropillar compression deformation of Mo single crystals, Int. J. Plast. 92 (Suppl. C) (2017) S45–S56.
[66] W.S. Choi, S. Sandlöbes, N.V. Malyar, C. Kirchlechner, S. Korte-Kerzel, G. Dehm, B.C. De Cooman, D. Raabe, Dislocation interaction and twinning-induced plasticity in face-centered cubic Fe-Mn-C micro-pillars, Acta Mater. 132 (Suppl. C) (2017) S162–S173.
[67] K.A. Afanasyev, F. Sansoz, Strengthening in gold nanopillars with nanoscale twins, Nano Lett. 7 (7) (2007) 2056–2062.
[68] D. Kiener, A.M. Minor, Source-controlled yield and hardening of Cu(100) studied by in situ transmission electron microscopy, Acta Mater. 59 (4) (2011) 1328–1337.
[69] A.T. Jennings, J. Li, J.R. Greer, Emergence of strain-rate sensitivity in Cu nanopillars: transition from dislocation multiplication to dislocation nucleation, Acta Mater. 59 (14) (2011) 5627–5637.
[70] D. Jang, X. Li, H. Gao, J.R. Greer, Deformation mechanisms in nanotwinned metal nanopillars, Nat. Nano 7 (9) (2012) 594–601.
[71] F. Hammami, Y. Kulkarni, Size effects in twinned nanopillars, J. Appl. Phys. 116 (3) (2014) 033512.
[72] M.A. Shehadeh, H.M. Zbib, T. Diaz de la Rubia, Multiscale dislocation dynamics simulations of shock compression in copper single crystal, Int. J. Plast. 21 (12) (2005) 2369–2390.
[73] J.R. Greer, J.T.M. De Hosson, Plasticity in small-sized metallic systems: intrinsic versus extrinsic size effect, Prog. Mater. Sci. 56 (6) (2011) 654–724.
[74] C.R. Mayer, L.W. Yang, S.S. Singh, J. Llorca, J.M. Molina-Aldareguia, Y.L. Shen, N. Chawla, Anisotropy, size, and aspect ratio effects on micropillar compression of AlSiC nanolaminate composites, Acta Mater. 114 (2016) 25–32.
[75] R. Fritz, V. Maier-Kiener, D. Lutz, D. Kiener, Interplay between sample size and grain size: single crystalline vs. ultrafine-grained chromium micropillars, Mater. Sci. Eng.: A 674 (Suppl. C) (2016) S626–S633.
[76] C. Howard, D. Frazer, A. Lupinacci, S. Parker, R.Z. Valiev, C. Shin, B. William Choi, P. Hosemann, Investigation of specimen size effects by in-situ microcompression of equal channel angular pressed copper, Mater. Sci. Eng.: A 649 (Suppl. C) (2016) S104–S113.
[77] F. Hammami, Y. Kulkarni, Rate dependence of grain boundary sliding via time-scaling atomistic simulations, J. Appl. Phys. 121 (8) (2017) 085303.
[78] X.W. Zhou, R.A. Johnson, H.N.G. Wadley, Misfit-energy-increasing dislocations in vapor-deposited CoFe/NiFe multilayers, Phys. Rev. B 69 (14) (2004) 144113.
[79] S. Plimpton, Fast parallel algorithms for short-range molecular dynamics, J. Comput. Phys. 117 (1) (1995) 1–19.
[80] A. Stukowski, Visualization and analysis of atomistic simulation data with OVITO–the open visualization tool, Model. Simul. Mater. Sci. Eng. 18 (1) (2010) 015012.
[81] A. Stukowski, V.V. Bulatov, A. Arsenlis, Automated identification and indexing of dislocations in crystal interfaces, Model. Simul. Mater. Sci. Eng. 20 (8) (2012) 085007.
[82] J.R. Greer, W.D. Nix, Nanoscale gold pillars strengthened through dislocation starvation, Phys. Rev. B 73 (24) (2006) 245410.
[83] W.A. Jesser, J.W. Matthews, Pseudomorphic deposits of cobalt on copper, Philos. Mag.: A J. Theor. Exp. Appl. Phys. 17 (147) (1968) 461–473.
[84] Y. Kulkarni, R.J. Asaro, Are some nanotwinned fcc metals optimal for strength, ductility and grain stability? Acta Mater. 57 (16) (2009) 4835–4844.
[85] T. Zhu, J. Li, A. Samanta, H.G. Kim, S. Suresh, Interfacial plasticity governs strain rate sensitivity and ductility in nanostructured metals, Proc. Natl. Acad. Sci. USA 104 (9) (2007) 3031–3036.
[86] Z.-J. Wang, Q.-J. Li, Z.-W. Shan, J. Li, J. Sun, E. Ma, Sample size effects on the large strain bursts in submicron aluminum pillars, Appl. Phys. Lett. 100 (7) (2012) 071906.
[87] S.H. Oh, M. Legros, D. Kiener, G. Dehm, In situ observation of dislocation nucleation and escape in a submicrometre aluminium single crystal, Nat. Mater. 8 (2) (2009) 95–100.
[88] F.F. Csikor, C. Motz, D. Weygand, M. Zaiser, S. Zapperi, Dislocation avalanches, strain bursts, and the problem of plastic forming at the micrometer scale, Science 318 (5848) (2007) 251–254.